

Thermoelectric performance of functionalized Sc₂C MXenes

S. Kumar and U. Schwingenschlöggl*

King Abdullah University of Science and Technology, Physical Science and Engineering Division, Thuwal 23955-6900, Saudi Arabia

(Received 9 March 2016; revised manuscript received 14 June 2016; published 5 July 2016)

Functionalization of the MXene Sc₂C, which has the rare property to realize semiconducting states for various functionalizations including O, F, and OH, is studied with respect to the electronic and thermal behavior. The lowest lattice thermal conductivity is obtained for OH functionalization and an additional 30% decrease can be achieved by confining the phonon mean free path to 100 nm. Despite a relatively low Seebeck coefficient, Sc₂C(OH)₂ is a candidate for intermediate-temperature thermoelectric applications due to compensation by a high electrical conductivity and very low lattice thermal conductivity.

DOI: [10.1103/PhysRevB.94.035405](https://doi.org/10.1103/PhysRevB.94.035405)

I. INTRODUCTION

A large family of two-dimensional materials, the MXenes, can be prepared from the MAX phases by exfoliation in aqueous hydrofluoric acid using ultrasonic methods [1]. The bulk materials have a layered structure (space group $P6_3/mmc$) with chemical formula $M_{n+1}AX_n$, where $n = 1, 2, \text{ or } 3$; M is an early transition metal; A is a group 13/14 element; and X = N or C. MXenes contain M and X atoms in $(n+1):n$ ratio. During the exfoliation process the A atoms are replaced by O, F, and/or OH, leading to functionalized MXenes $M_{n+1}X_nT_2$ with termination T. So far functionalization has been demonstrated for the MXenes Ti₂C, Ti₃C₂, Ti₃CN, Ta₄C₃, Nb₂C, V₂C, (Ti_{1/2}Nb_{1/2})₂C, and (V_{1/2}Cr_{1/2})₂C, being of interest for a variety of applications in energy storage and capacitive devices [2,3]. A change in resistance on selective intercalation additionally indicates potential in chemical sensing [4].

Thermoelectric devices can provide clean solutions to energy demands by power generation out of waste heat and electrical cooling, for example [5]. The thermoelectric efficiency of a material is given by the dimensionless figure of merit, $zT = S^2\sigma T/\kappa$, where T is the temperature, S is the Seebeck coefficient, σ is the electrical conductivity, and κ is the thermal conductivity with electronic (κ_e) and lattice (κ_l) contributions. In contrast to the metallic $M_{n+1}AX_n$ phases, most MXenes show finite band gaps and high S values [6]. Optimization of zT often suffers from interdependence between σ and κ_e through the Wiedemann-Franz relation, $\kappa_e = L\sigma T$, L being the Lorenz number. While typically the power factor ($S^2\sigma$) is used to evaluate the thermoelectric potential of a material, a complete picture requires studying the electronic as well as thermal transport. We adopt this approach to address Sc₂C, as this MXene realizes semiconducting states for various functionalizations including O, F, and OH.

II. THEORETICAL APPROACH

We use density functional theory based on a plane-wave basis and the projector augmented wave approach, as implemented in the Vienna *ab initio* Simulation Package [7]. A kinetic-energy cutoff of 500 eV and the generalized gradient

approximation [8] for the exchange-correlation potential are used. Employing a Γ -centred $12\times 12\times 1$ \mathbf{k} mesh, the model structures are relaxed until the atomic forces have declined to less than 5 meV/Å with an energy convergence of 10^{-6} eV. Three-dimensional periodic boundary conditions combined with a 15-Å-thick vacuum region along the z direction give rise to monolayer structures. A $48\times 48\times 1$ \mathbf{k} mesh and the tetrahedron method are used to compute the density of states (DOS). The thermoelectric transport is studied using semiclassical Boltzmann theory and the rigid band approach (BOLTZTRAP code) [9] with the constant relaxation-time approximation [10]. The electronic structure is recalculated on a dense $60\times 60\times 1$ \mathbf{k} mesh (3972 points) for the Fourier interpolation of the Kohn-Sham eigenvalues that is used to obtain derivatives. The only empirical parameter in our approach is the electronic relaxation time, which has been estimated in Ref. [6] to be about $\tau = 10$ fs by comparing theoretical values of σ/τ to experimental values of σ for a range of MAX phases. Its weak temperature dependence is neglected. In this sense, the calculated figures of merit constitute upper bounds.

The thermal transport by phonons is studied by means of the Boltzmann transport equation [11,12] with the second- and third-order interatomic force constants as input (SHENGBTE code) [13–15]. Crystal symmetry and translational invariance are enforced in the determination of the harmonic force constants. Harmonic phonons are calculated using the PHONOPY code [16] with a $4\times 4\times 1$ supercell and $3\times 3\times 1$ \mathbf{k} mesh. For the third-order force constants a finite displacement method is used, where two atoms in the supercell are displaced simultaneously and the forces on the remaining atoms are calculated (imposing translational invariance). Interactions up to fourth nearest neighbors are considered for calculating the cubic force constants. The lattice thermal conductivity is evaluated as

$$\kappa_l^{\alpha\beta} = \frac{1}{k_B T^2 \Omega N} \sum_{\lambda} f_0(f_0 + 1) (\hbar\omega_{\lambda})^2 v_{\lambda}^{\alpha} v_{\lambda}^{\beta}, \quad (1)$$

where k_B is the Boltzmann constant, T is the temperature, Ω is the volume of the unit cell, N is the number of points used to sample the \mathbf{q} space, f_0 is the equilibrium phonon distribution function, \hbar is the reduced Planck constant, λ is the phonon mode (comprising the phonon branch index and wave number), ω_{λ} is the angular frequency, v_{λ} is the group velocity,

*udo.schwingenschlöggl@kaust.edu.sa

TABLE I. Structural parameters (Å or deg) and band gaps (eV).

	a	C-T	Sc-C	Sc-T	$\angle\text{TScT}$	$\angle\text{CScC}$	Band gap
Sc_2CO_2	3.430	1.65	2.20	2.10	110	102	1.84 (indirect, Γ -K)
Sc_2CF_2	3.281	3.10	2.28	2.21	96	92	1.03 (indirect, Γ -M)
$\text{Sc}_2\text{C}(\text{OH})_2$	3.305	3.15	2.29	2.28	93	93	0.44 (direct, Γ)

and \mathbf{F}_λ is the mean free displacement [15]. In the following we will discuss $\kappa_l = \kappa_l^{xx} = \kappa_l^{yy}$. A $60 \times 60 \times 1$ \mathbf{q} mesh (3600 points) is employed and shows a tolerance of less than 0.5% for κ_l of Sc_2CO_2 with respect to a $100 \times 100 \times 1$ \mathbf{q} mesh, for example. The Dirac δ functions for energy conservation in phonon processes are approximated by Gaussian functions with local adaptive broadening [14]. To calculate Ω , layer thicknesses of 5.73, 6.76, and 7.40 Å are used for Sc_2CO_2 , Sc_2CF_2 , and $\text{Sc}_2\text{C}(\text{OH})_2$, respectively [17].

III. RESULTS AND DISCUSSION

Studying O, F, and OH functionalization on both sides of Sc_2C , we find that $\text{T} = \text{O}$ results in a qualitatively different structure than $\text{T} = \text{F}$ or OH with short C-T distance (see Table I and Fig. 1). This difference is also reflected by shorter Sc-C and Sc-T bond lengths and larger $\angle\text{TScT}$ and $\angle\text{CScC}$ bond angles in Sc_2CO_2 , because the proximity of O to C results in a charge redistribution that strengthens the Sc-C bond. Both the band-gap size and character differ significantly between the three functionalizations; see the right column of Table I and the electronic band structures

in Fig. 2. Since for O/F functionalization the conduction-band minimum is formed by the Sc $3d$ bands and for OH functionalization by the O $2p$ bands, we obtain in the latter case a direct band gap with significantly reduced size. We note that the electronic dispersion relations of functionalized Sc_2C previously have been determined in Refs. [6,17], showing qualitative agreement with our results. Beyond, the sizes of our band gaps agree with Ref. [6], except for $\text{Sc}_2\text{C}(\text{OH})_2$, while the hybrid functional calculations of Ref. [17] result in higher values but reproduce the trends observed in our study.

Flat bands at the Fermi level are favorable for thermoelectric purposes as they lead to high S values [18]. Table II indicates that the average heat carried per hole (a measure of S) is larger for O/F than for OH functionalization. According to Figs. 3(a)–3(f), S decreases for increasing carrier concentration, which agrees with the Pisarenko relation [19]

$$S = \frac{8\pi^2 k_B^2}{3eh^2} m^* T \left(\frac{\pi}{3\rho} \right)^{3/2}, \quad (2)$$

where m^* and ρ are the effective mass and carrier concentration, respectively. We note that a temperature of 900 K should be well accessible for MXenes [20]. The value of ρ is calculated by integrating the DOS up to the required chemical potential for some doping at a given temperature. While high temperature should favor S , we find for low carrier concentration a reduction due to bipolar conduction (significant amount of minority carriers). The smaller the band gap, the larger is this effect. Table II includes a comparison with the transition-metal dichalcogenides MoSe_2 and WSe_2 [21]. Heavier holes (majority carriers) in Sc_2CO_2 and Sc_2CF_2 than in MoSe_2 and WSe_2 enhance S . For $\text{Sc}_2\text{C}(\text{OH})_2$ the holes are also heavier but at the same time the size of the band gap is strongly reduced, which together results in comparable values of S . As expected, σ grows with ρ [see Figs. 3(g)–3(l)]. Comparison to the third and fourth columns of Table II shows that the relative magnitudes obtained for different functionalizations are influenced by details of the band dispersions and cannot be predicted from the effective masses alone. The degenerate hole pockets at the Γ point enhance σ without negatively affecting S [22]. According to Figs. 4(a)–4(f) the three compounds show similar values of $S^2\sigma$ and according to Figs. 4(g)–4(l) the trends of κ_e reproduce those observed for σ in Figs. 3(g)–3(l).

Phonon dispersion relations along the high-symmetry directions of the Brillouin zone are shown in Fig. 5. We find no imaginary frequencies, indicating stability of the functionalizations. $\text{T} = \text{O}$ leads to lower frequencies than $\text{T} = \text{F}$ or OH (especially for the acoustic branches determining the thermal transport) as expected from the lattice constants given in Table I. The acoustic branches show large group velocities (given in Table III for the flexural, transversal, and longitudinal branches) and similarity of the Γ -M and Γ -K directions,

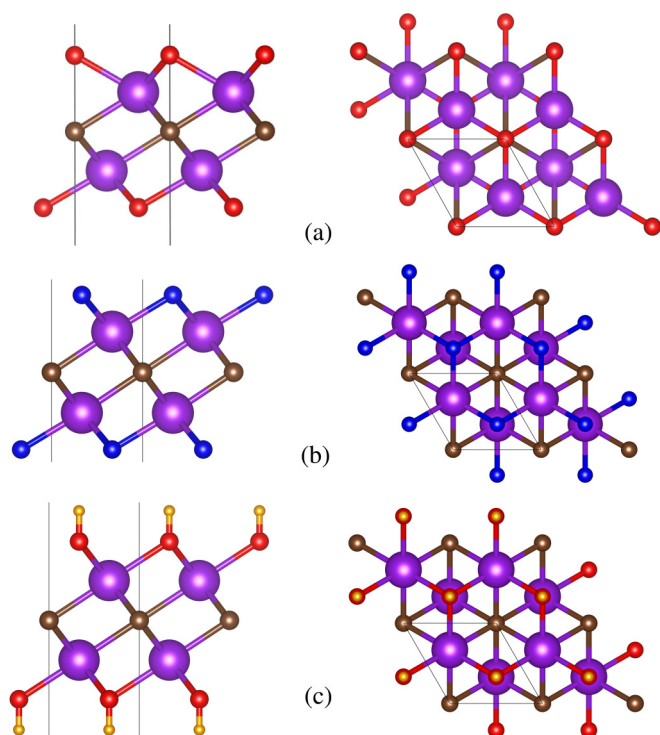


FIG. 1. Atomic structure: Side and top views of monolayer Sc_2C functionalized by (a) O, (b) F, and (c) OH. Color code: Sc pink, C brown, O red, F blue, and H yellow.

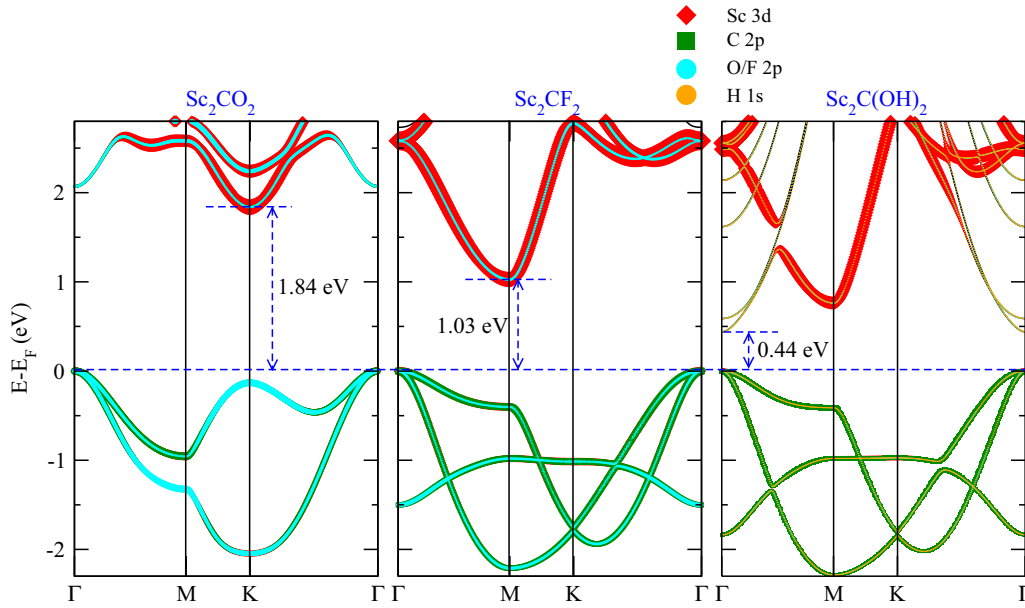


FIG. 2. Band structures with orbital weights.

representing isotropic in-plane elastic response. The special structure of Sc_2CO_2 is reflected by deviations in v_{ZA} and v_{TA} from the other two functionalizations.

The values of κ_l calculated in the single mode relaxation time approximation (SMRTA) are found to be smaller than those obtained from the iterative approach based on self-consistent phonon lifetimes [see Figs. 6(a)–6(c)]. The difference amounts to around 15% at room temperature, indicating dominance of Umklapp processes over normal processes. In each case the difference decreases when the temperature increases, because the weight of Umklapp processes in κ_l grows for decreasing phonon wavelengths. The normal processes, however, provide indirect resistance to the thermal flow by modifying the distribution of the Umklapp processes and therefore lower κ_l [23]. As the iterative procedure is more accurate than the SMRTA, it is used to calculate zT .

The finite band gaps lead to appreciable Born effective charges (Z^*) and dielectric constants (ϵ_∞) (see Table III). The resulting long-range electrostatic interactions cause a splitting of the longitudinal optical (LO) and transverse optical (TO) branches. However, this splitting modifies κ_l only slightly (less than 3%). It may be noted that $\text{T} = \text{OH}$ leads to high-frequency optical branches near 3760 cm^{-1} (close to the O-H infrared frequency [24]), a feature that can be used to characterize the

level of OH functionalization (as typically various functional groups are present simultaneously [2]).

Separating the acoustic and optical contributions to κ_l , we find the former to be smaller than in other two-dimensional

TABLE II. Seebeck coefficients at room temperature without doping ($\mu\text{V K}^{-1}$) and effective masses (m_e).

	S	Electron	Hole
Sc_2CO_2	1022	0.86 (K)	1.06 (Γ)
Sc_2CF_2	1036	0.92 (M)	2.35 (Γ)
$\text{Sc}_2\text{C(OH)}_2$	372	0.57 (Γ)	1.87 (Γ)
MoSe_2	427	0.54 (K)	0.64 (K)
WSe_2	350	0.34 (K)	0.44 (K)

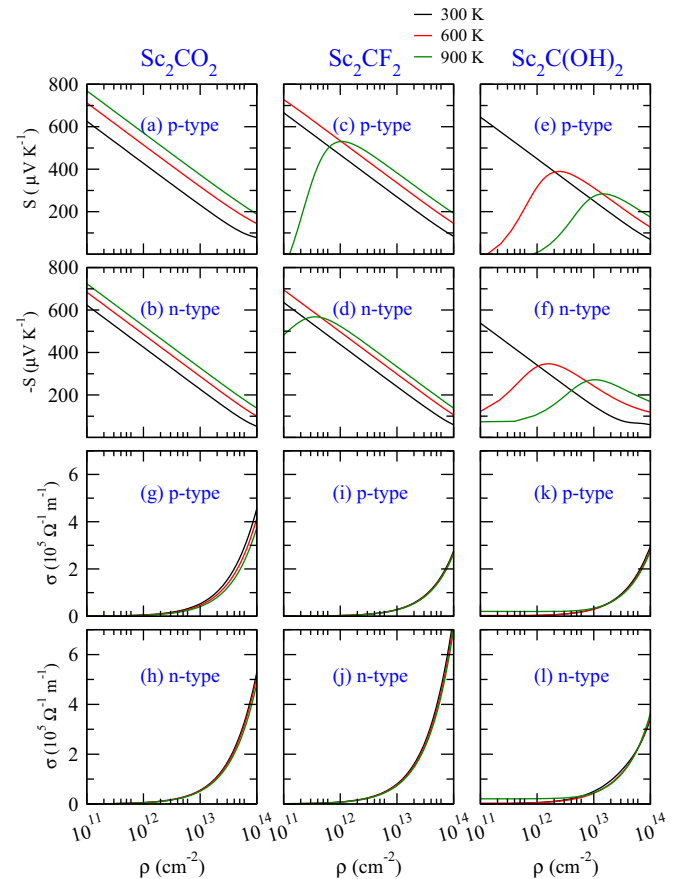


FIG. 3. Seebeck coefficients and electrical conductivities.

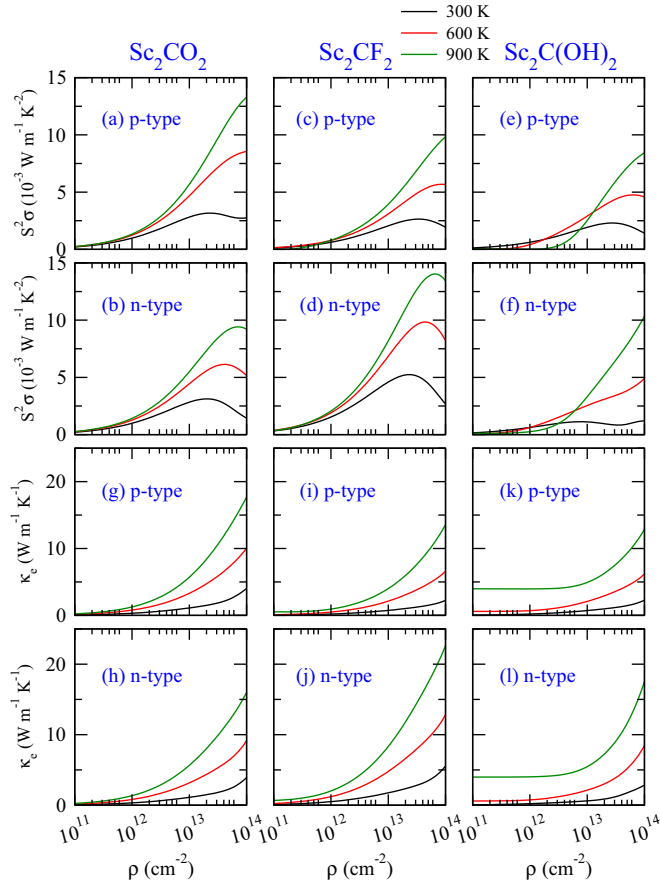


FIG. 4. Thermoelectric power factors and electronic thermal conductivities.

materials such as graphene [25], blue phosphorene [26], MoS₂ [27], and MoSe₂ and WSe₂ [21] at room temperature (see Table IV). Overlap of the acoustic and optical branches for T = F and OH (see Fig. 5) enhances three-phonon interactions and thus lowers κ_l . We note that additional optical branches appear at high frequency for OH functionalization but give negligible contributions to κ_l (<0.4%). Relatively high anharmonic phonon scattering rates for T = OH [see Figs. 6(d)–6(f)], calculated using Fermi’s golden rule, also lower κ_l , as the phonon relaxation times are reduced (slow thermal transport). It turns out that in the materials under study κ_l is significantly higher than the in-plane value of Bi₂Te₃

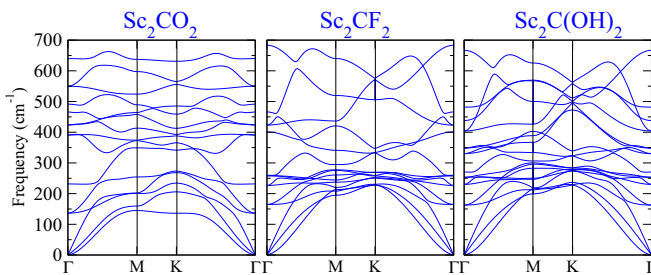


FIG. 5. Phonon dispersion relations. Additional optical branches appear at higher energy for OH functionalization.

TABLE III. Group velocities of the acoustic branches (km s⁻¹) in the long-wavelength limit, in-plane Born effective charges (electrons), and dielectric constants.

	v_{ZA}	v_{TA}	v_{LA}	Z_{Sc}^*	Z_C^*	$Z_{O/F}^*$	Z_H^*	ϵ_∞
Sc ₂ CO ₂	1.8	3.1	8.7	3.57	-2.77	-2.18		2.51
Sc ₂ CF ₂	1.2	5.1	8.7	4.29	-5.21	-1.69		3.34
Sc ₂ C(OH) ₂	1.0	5.2	8.9	4.46	-5.69	-1.90	0.28	4.62

(1.3 W m⁻¹ K⁻¹) [28], because the involved elements are less heavy.

The dependence of zT on ρ as shown in Fig. 7 is characterized by maxima around 4×10^{-13} cm⁻². For both p - and n -type carriers the values grow from Sc₂CO₂ to Sc₂C(OH)₂ at high ρ as κ_l is reduced. The opposite trend is observed at low ρ , since κ_e grows from T = F to OH [see Figs. 4(g)–4(l)]. We note that the mixed grain approach can be used to lower κ_e [29]. Being close to C/N in the periodic table, O is the most probable substitutional dopant for MXenes, which is well known for the MAX phases [30,31]. Since the thermoelectric response can be enhanced (without altering the chemical composition) by restricting the phonon wavelength via grain boundaries [32], we calculate the cumulative lattice thermal conductivity, $\kappa_l^c = \sum_{|v_\lambda| \tau_\lambda \leq \Lambda} \kappa_l$, where Λ is the maximum phonon mean free path. Restriction of the phonons to 100 nm, for example, leads to a 30% reduction of κ_l , at room temperature for all the functionalized MXenes

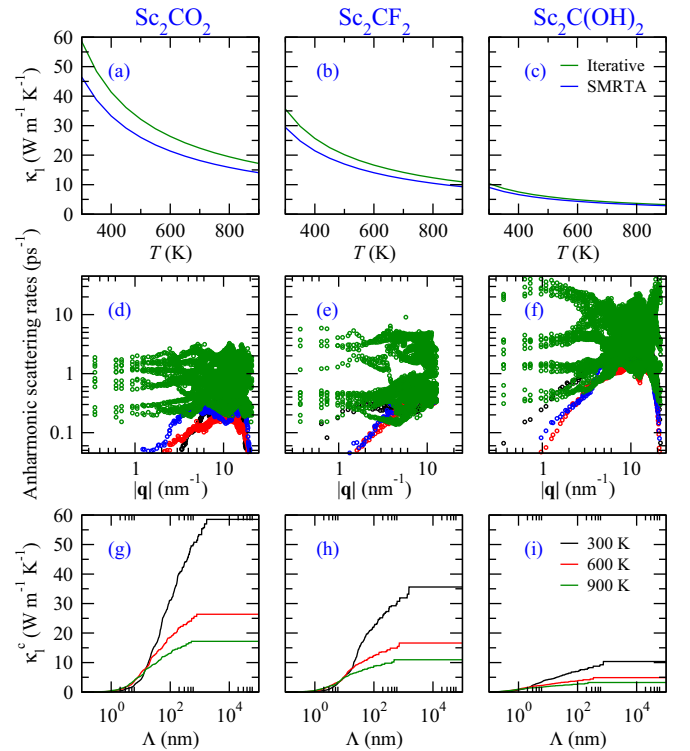


FIG. 6. Lattice thermal conductivities, room-temperature anharmonic scattering rates (black, red, blue, and green color refers to the ZA, TA, LA, and optical branches, respectively), and cumulative lattice thermal conductivities.

TABLE IV. Lattice thermal conductivity and contribution of the acoustic phonon branches ($\text{W m}^{-1} \text{K}^{-1}$). Data for graphene ($10\text{-}\mu\text{m}$ sample), blue phosphorene, MoS_2 ($10\text{-}\mu\text{m}$ sample), MoSe_2 ($1\text{-}\mu\text{m}$ sample), and WSe_2 ($1\text{-}\mu\text{m}$ sample) at room temperature are given for comparison.

	κ_l	$\kappa_l^{\text{acoustic}}$
Sc_2CO_2	59	48
Sc_2CF_2	36	30
$\text{Sc}_2\text{C(OH)}_2$	10	8
Graphene	3600	3564
Blue phosphorene	78	76
MoS_2	108	98
MoSe_2	69	69
WSe_2	43	42

under consideration [see Figs. 6(g)–6(i)]. We note that the maximal electronic mean free path in the materials under study is below 11 nm, so that κ_e will not be affected by such nanostructuring.

IV. CONCLUSION

The thermoelectric behavior of the MXene Sc_2C functionalized by O, F, and OH groups has been investigated taking into account the electron and phonon dynamics by density functional theory and the Boltzmann transport formalism. The functionalization significantly affects the structural properties and electronic band structure. In particular, the small direct band gap in the case of OH functionalization is attributed to the fact that O $2p$ states form the conduction-band minimum. Though the Seebeck coefficient is significantly smaller for OH than for O/F functionalization at high temperature, the power factor remains significant due to compensation by a high electrical conductivity. Moreover, the Seebeck coefficient for OH functionalization can be enhanced by suppressing the bipolar conduction at elevated temperature, for example, by tuning the band gap via strain. The large electronic contribution to the thermal conductivity obtained for OH functionalization

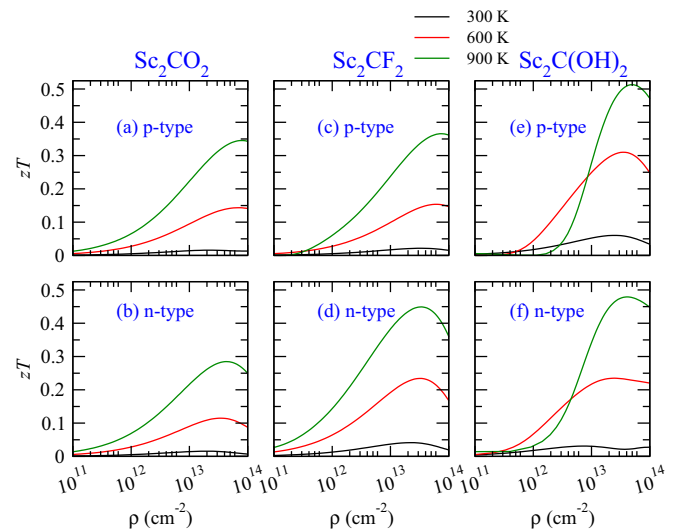


FIG. 7. Figures of merit.

at small carrier concentration can be reduced by the mixed grain approach.

Since the acoustic phonon branches turn out to contribute less than in graphene, blue phosphorene, MoS_2 , MoSe_2 , and WSe_2 , for example, the lattice thermal conductivity is small. For O and F functionalization the figure of merit can be strongly enhanced by lowering the lattice thermal conductivity, since the power factor is high. The fact that the best thermoelectric response is obtained for OH functionalization is due to the lowest lattice thermal conductivity in this case (largest anharmonic phonon scattering). Finally, the possibility to enhance the figure of merit by means of phonon confinement has been addressed from a quantitative perspective.

ACKNOWLEDGMENT

The research reported in this publication was supported by funding from King Abdullah University of Science and Technology (KAUST).

- [1] M. Naguib, M. Kurtoglu, V. Presser, J. Lu, J. Niu, M. Heon, L. Hultman, Y. Gogotsi, and M. W. Barsoum, *Adv. Mater.* **23**, 4248 (2011).
- [2] M. Naguib, V. N. Mochalin, M. W. Barsoum, and Y. Gogotsi, *Adv. Mater.* **26**, 992 (2014).
- [3] Z. Ling, C. E. Ren, M.-Q. Zhao, J. Yang, J. M. Giammarco, J. Qiu, M. W. Barsoum, and Y. Gogotsi, *Proc. Natl. Acad. Sci. USA* **111**, 16676 (2014).
- [4] J. Chen, K. Chen, D. Tong, Y. Huang, J. Zhang, J. Xue, Q. Huang, and T. Chen, *Chem. Commun.* **51**, 314 (2015).
- [5] T. M. Tritt, *Annu. Rev. Mater. Res.* **41**, 433 (2011).
- [6] M. Khazaei, M. Arai, T. Sasaki, M. Estili, and Y. Sakka, *Phys. Chem. Chem. Phys.* **16**, 7841 (2014).
- [7] G. Kresse and D. Joubert, *Phys. Rev. B* **59**, 1758 (1999).
- [8] J. P. Perdew, K. Burke, and M. Ernzerhof, *Phys. Rev. Lett.* **77**, 3865 (1996).
- [9] G. Madsen and D. Singh, *Comput. Phys. Commun.* **175**, 67 (2006).
- [10] L. Chaput, P. Pécœur, and H. Scherrer, *Phys. Rev. B* **75**, 045116 (2007).
- [11] D. A. Broido, M. Malorny, G. Birner, N. Mingo, and D. A. Stewart, *Appl. Phys. Lett.* **91**, 231922 (2007).
- [12] A. Ward, D. A. Broido, D. A. Stewart, and G. Deinzer, *Phys. Rev. B* **80**, 125203 (2009).
- [13] W. Li, L. Lindsay, D. A. Broido, D. A. Stewart, and N. Mingo, *Phys. Rev. B* **86**, 174307 (2012).
- [14] W. Li, N. Mingo, L. Lindsay, D. A. Broido, D. A. Stewart, and N. A. Katcho, *Phys. Rev. B* **85**, 195436 (2012).
- [15] W. Li, J. Carrete, N. A. Katcho, and N. Mingo, *Comput. Phys. Commun.* **185**, 1747 (2014).
- [16] A. Togo, F. Oba, and I. Tanaka, *Phys. Rev. B* **78**, 134106 (2008).

- [17] X.-H. Zha, K. Luo, Q. Li, Q. Huang, J. He, X. Wen, and S. Du, *Europhys. Lett.* **111**, 26007 (2015).
- [18] G. D. Mahan and J. O. Sofo, *Proc. Natl. Acad. Sci. USA* **93**, 7436 (1996).
- [19] G. J. Snyder and E. S. Toberer, *Nat. Mater.* **7**, 105 (2008).
- [20] Z. Li, L. Wang, D. Sun, Y. Zhang, B. Liu, Q. Hu, and A. Zhou, *Mater. Sci. Eng. B* **191**, 33 (2015).
- [21] S. Kumar and U. Schwingenschlögl, *Chem. Mater.* **27**, 1278 (2015).
- [22] Y. Pei, X. Shi, A. LaLonde, H. Wang, L. Chen, and G. J. Snyder, *Nature (London)* **473**, 66 (2011).
- [23] P. Carruthers, *Rev. Mod. Phys.* **33**, 92 (1961).
- [24] G. Socrates, *Infrared and Raman Characteristic Group Frequencies: Tables and Charts* (Wiley, New York, 2004).
- [25] L. Lindsay, W. Li, J. Carrete, N. Mingo, D. A. Broido, and T. L. Reinecke, *Phys. Rev. B* **89**, 155426 (2014).
- [26] A. Jain and A. J. H. McGaughey, *Sci. Rep.* **5**, 8501 (2015).
- [27] W. Li, J. Carrete, and N. Mingo, *Appl. Phys. Lett.* **103**, 253103 (2013).
- [28] O. Hellman and D. A. Broido, *Phys. Rev. B* **90**, 134309 (2014).
- [29] L.-D. Zhao, B.-P. Zhang, W.-S. Liu, and J.-F. Li, *J. Appl. Phys.* **105**, 023704 (2009).
- [30] P. O. Å. Persson, J. Rosén, D. R. McKenzie, and M. M. M. Bilek, *Phys. Rev. B* **80**, 092102 (2009).
- [31] J. Rosen, M. Dahlqvist, S. I. Simak, D. R. McKenzie, and M. M. M. Bilek, *Appl. Phys. Lett.* **97**, 073103 (2010).
- [32] T. H. Ly, M.-H. Chiu, M.-Y. Li, J. Zhao, D. J. Perello, M. O. Cichocka, H. M. Oh, S. H. Chae, H. Y. Jeong, F. Yao *et al.*, *ACS Nano* **8**, 11401 (2014).